Effect of compression on the water management of polymer electrolyte fuel cells: An in-operando neutron radiography study

Y. Wu,[a] J. I. S. Cho,[a,b] X. Lu,[a] L.Rasha,[a] T. P. Neville,[a] J. Millichamp,[a] R. Ziesche,[a] N. Kardjilov,[c] H. Markötter, [c] P. Shearing,[a]* D. J. L. Brett[a]*

---

[a]*Electrochemical Innovation Lab, Department of Chemical Engineering, University College London, London WC1E 7JE, United Kingdom.*
[b]*EPSRC "Frontier Engineering" Centre for Nature Inspired Engineering & Department of Chemical Engineering, University College London, London WC1E 7JE,United Kingdom.*
[c]*Helmholtz-Zentrum Berlin (HZB), Hahn-Meitner-Platz 1, 14109 Berlin, Germany*

Email: d.brett@ucl.ac.uk (D. J. L. Brett); p.shearing@ucl.ac.uk (P. Shearing)

Abstract

In-depth understanding of the effect of compression on the water management in polymer electrolyte fuel cells (PEFCs) is indispensable for optimisation of performance and durability. Here, in-operando neutron radiography is utilised to evaluate the liquid water distribution and transport within a PEFC under different levels of compression. A quantitative analysis is presented with the influence of compression on the water droplet number and median droplet surface area across the entire electrode area. Water management and performance of PEFCs is strongly affected by the compression: the cell compressed at 1.0 MPa demonstrates ~3.2% and ~7.8% increase in the maximum power density over 1.8 MPa and 2.3 MPa, respectively. Correlation of performance to neutron radiography reveals that the performance deviation in the mass transport region is likely due to flooding issues. This could be ascribed to the loss of the porosity and increased tortuosity factor of the gas diffusion layer under the land at higher compression pressure. The size and number of droplets formed as a function of cell compression was examined: with higher compression pressure, water droplet number and median droplet surface area rapidly increase, showing the ineffective water removal, which leads to fuel starvation and the consequent performance decay.

Keywords: Compression; water management; neutron imaging; gas diffusion layer; droplet; porosity.

1. Introduction

Polymer electrolyte fuel cells (PEFCs) operating on hydrogen have several advantages compared to conventional hydrocarbon-based power sources. They have shown significant advances in terms of performance, efficiency and durability for a wide range of applications. However, there is scope for further improvements. One of the long-standing challenges to ensuring efficient and reliable fuel cell performance is accomplishing effective internal water management [1]-[3].

PEFCs require adequate compression to reduce the contact resistance, primarily between the flow-field lands and the gas diffusion layer (GDL) [4]. Low compression pressure can cause high contact resistance and gas leakage. On the other hand, excessive compression can lead to higher mass transfer resistance, resulting in deteriorated cell performance [5]. Thus, an in-depth understanding of the compression effect is required for optimisation of PEFC performance.

Different methods have been applied to study the compression effects on PEFCs. Polarisation tests [6]-[8] have shown that the fuel cell performance has a strong dependence on compression, with generally a lower performance observed at higher (excess) compressions. Electrochemical impedance spectroscopy (EIS) has been applied to distinguish and separate the different loss mechanisms of the fuel cell system under different compression states [5] [9]. Generally, high compression ratio results in lower high-frequency resistance due to lower contact resistance, whereas the low-frequency resistance increases, as a result of depreciated mass transport.

During the compression process, GDL undergoes a significant morphological change [4], [5]. X-ray computed tomography (XCT) allows one to resolve the internal structure and inhomogeneity under controlled conditions. This method has been used to analyse the effects of compression on the morphological properties of GDL materials, such as porosity, pore size distribution, and tortuosity [10]-[13]. Studies report that the porosity of GDLs decreased with compression, leading to reduction in mass transport properties and subsequent cell performance. Numerical simulations have been applied to investigate the compression effect. Pore networks extracted from synchrotron-based micro-computed tomography images of compressed GDLs [14] were employed to simulate liquid water transport in GDL materials over a range of compression pressures. They reported an optimum compression state for Toray

GDL material with respect to water management and oxygen diffusion, which are directly associated with the performance of the PEFC. XCT was used to determine the GDL morphology, which was then used to generate the pore-network realizations for the numerical model [15]. Their investigations show that doubling the anode GDL thickness with the increase in interior porosity (similar to the lower compression ratio) allows more liquid water transport through the membrane and out of the anode. X-ray micro-tomography has been combined with Lattice Boltzmann numerical modelling [16] to analyse the pore-scale water transport behaviour under different compression levels. They suggested that the internal pressure exerted on the carbon cloth GDL should be within 0.3-10.0 MPa to achieve the optimum transport properties of a PEFC. Above this range, the in-plane and through-plane permeability of the GDL decrease. In addition to this, several authors have used ex-situ techniques (e.g., XCT [17], synchrotron X-ray imaging [18], optical visualisation [19] and fluorescence microscopy [20]) to visualise water content within the compressed GDL. The results indicated reduced water saturation within the GDL at lower compression ratio.

However, an in-depth study of the compression effect on the water distribution and transport within operating PEFCs has not been established. Having access to bespoke in-situ and in-operando diagnostic techniques capable of studying internal water dynamics is key to optimising components and operating conditions. Of the numerous PEFC water-mapping methods available, neutron imaging is arguably the most powerful. The high attenuation of neutrons by water [21] and high transparency of neutrons to other PEFC components, allow for high-resolution measurements of liquid water formation and transport across the active area. First pioneered by Mosdale et al. in 1996 [22], this technique has been employed to visualise water in PEFCs for different flow-field designs, current density, temperature, stoichiometry and relative humidity [23]-[30].

In this work, in-operando neutron imaging is employed to provide a unique insight into the relationship between the compression pressure and the related internal water management issues. In particular, this study allows for a detailed quantitative investigation of the effect of compression on the water droplet number and median droplet surface area across the entire active area. Therefore, this study fills a gap

in the literature and for the first time provides a systematic comparison of the water management within a PEFC under different levels of compression.

2. Experimental

2.1. Fuel cell design

A closed-cathode PEFC with an active area of 25 cm^2 was designed for testing. The cell consisted of two aluminium current collectors, two graphite flow-fields (Schunk, Germany), a membrane electrode assembly (MEA), gaskets and two end-plates. The contact angle of the graphite flow-field surface was measured using a drop shape analyser (Kruss DSA 100, Germany). An 8 µL drop of deionised water was placed on the surface of a graphite sample and the static contact angle was measured using built-in fitting software. The graphite flow-field surface exhibited hydrophilic surface properties with a measured contact angle of 78.3°. The two current collectors and the anode end-plate were electroless gold plated to prevent corrosion. An 'exploded' view of the fuel cell components is shown in Fig. 1 (a).

A horizontal five-channel serpentine geometry was used for the cathode, and a vertical single-channel serpentine was used for the anode flow-field, which is shown in Fig. 1 (b). The width, land and channel depth were all 1 mm. A cross-flow configuration is applied for the gas feed. The anode stream was directed from the upper left to the lower right corner of the MEA, and the cathode flow direction was from the upper right to the lower left corner. A 70 µm thick sheet of gasket material (Tygaflor) was used at the interface between flow-fields/current collector and end-plates for electrical insulation. A Tygaflor sheet was used as gasket to seal the perimeter of the MEA.

The MEA was fabricated in-house by hot pressing Nafion 212 membrane (DuPont, USA) and ELE00162 Johnson Matthey gas diffusion electrodes (GDL coated with catalyst layer 0.4 mg Pt/cm^2 at both sides). The MEA was pressed at 130°C for 3 minutes with an applied pressure of 400 psi. The GDL contains a Micro Porous Layer (MPL) for enhanced performance of the GDL catalyst layer interface. The porosity through the medium is ~70% [31]. A laboratory X-ray CT system, ZEISS Xradia 520 Versa (Carl Zeiss, USA) was used to take a longitudinal direction X-ray orthoslice to show the MEA structure (Fig. 1 (c)). A source voltage of 40 kV and a field-of-view of 0.67×0.67 mm^2 were used

for the sample, giving a voxel size of 1.03 μm. A dense phase is observed in the middle region of orthoslice (Nafion content), and a surrounding much lighter phase (MPL and catalyst). The GDL is at the both top and bottom of this sample.
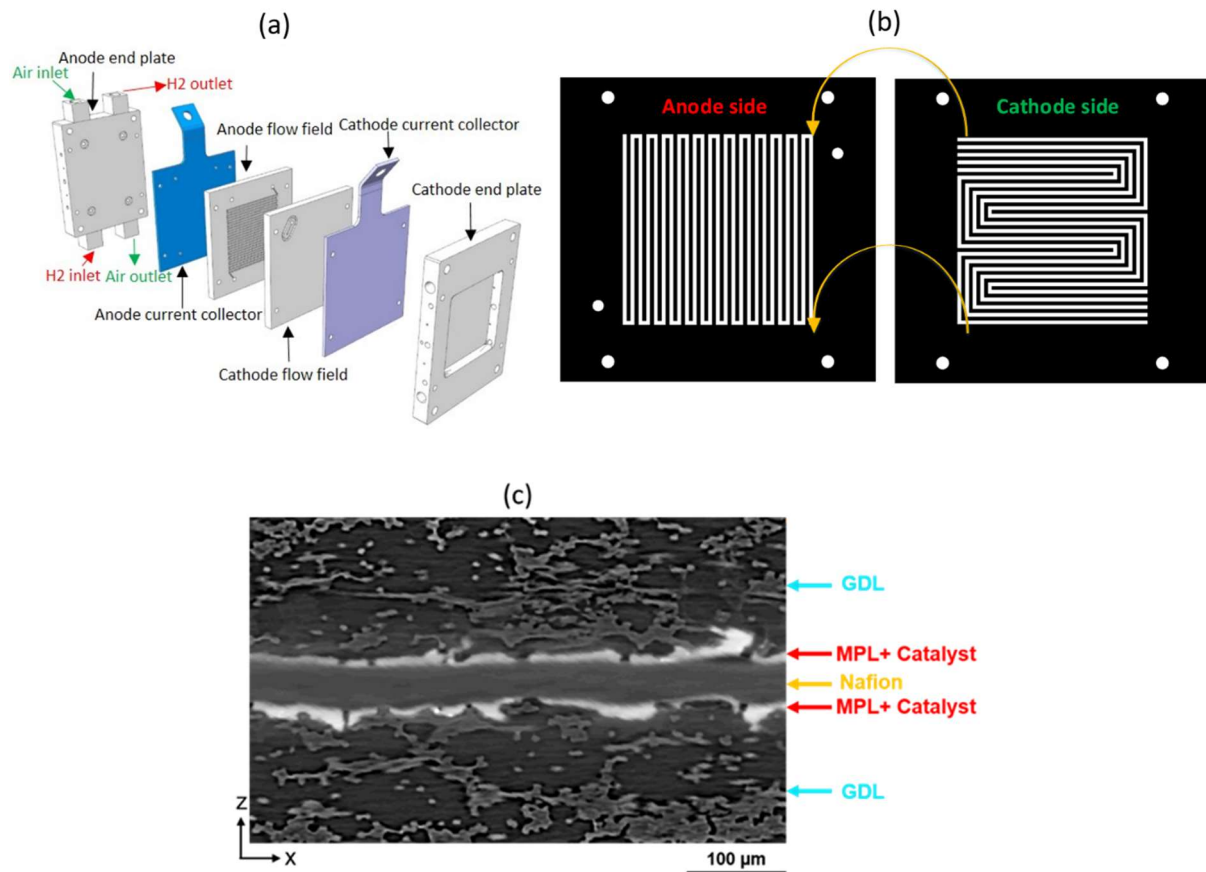

Fig. 1 (a) Exploded view of individual fuel cell components (excluding the MEA, which is between the flow-field plates; (b) anode and cathode flow-field designs. The channels of the anode flow-field were orientated vertically whereas the cathode flow-field channels were orientated horizontally; (c) X-ray orthoslice of made MEA.

2.2. Fuel cell compression process

Various compression methods have been established in the literature, such as springs, integrated bladders and hydraulic or pneumatic presses [4], [5]. However, by far the most commonly used technique is applying torque to tie-bolts at the end-plate to compress the PEFC.

Table 1-Parameter change of GDL before and after compression		
Compression pressure (MPa)	Thickness (μm)	Compression ratio (%)
0 (before compression)	210	0
1.0	175	16.7
1.8	155	26.2
2.3	145	31

To study the influence of compression on the water management, three fresh GDLs were compressed with three different torques; 1.4 Nm, 2.2 Nm and 3 Nm. The corresponding pressure value was measured using a pressure transducer (Omega, US) as 1.0 MPa, 1.8 MPa and 2.3 MPa, respectively. This agrees well with previously published works, which uses compression values in the range of 0.5 MPa -2.5 MPa for PEFC assembly [4], [5], [32], [33]. According to the test, 1.0 MPa is the minimum compression pressure for which no gas leaks occur in the current cell. The thickness change of the GDL can be used to estimate the change in porosity of the material. A micrometer (RS Pro, accuracy ±5 μm) was used to measure the changes in GDL thickness before and after compression (Table 1). The thickness of pristine GDL (after hot pressing but before compression) is 210 μm. Over the compression range of 1.0-2.3 MPa, the decrease in thickness of the GDL material observed equates to a compression ratio of ~31%, which is within the range previously reported for single PEFCs (10-60%) [5], [12] [17] [19] [20].

2.3 Fuel cell testing

In-house designed fuel cell rig and control software (LabVIEW, National Instruments, USA) were used to test PEFC (air, hydrogen, and the load) and record the data through communicating with a data acquisition card (DAQ card, USB 6363, National Instruments, USA). The PEFC was operated in the absence of gas humidification. Such operating parameters are chosen to alleviate excess flooding. The anode and cathode stoichiometric ratio were maintained at 1.5 and 2.5, respectively. The flow rates of gas inlets were controlled using two calibrated digital mass flow controllers (Bronkhorst, UK). The PEFC was operated at ambient temperature. The cell ohmic resistance was measured by Electrochemical Impedance Spectroscopy. The current was drawn from the fuel cell using a DC electronic load (PLZ664WA, Kikusui).

2.4 Neutron imaging

All experiments were conducted at the cold neutron radiography (CONRAD) beamline facility at Helmholtz-Zentrum Berlin (HZB). The beam is formed by a neutron guide and an additional collimation system, and is transmitted through the PEFC. The detector consisted of a CCD digital camera (Andor DW436N-BV) facing a LiF/ZnS neutron scintillator screen. The neutron scintillator converts neutron flux into light emission, which is then detected by the CCD camera. The cell was placed in through-plane orientation to the beam to visualise liquid water across the entire active area. An imaging field-of-view of 56×67 mm^2 with a pixel size of 26 μm was attained using the imaging set-up developed by Kardjilov et al.[34]. Each image was taken with an exposure time of 5 s.

To isolate generated liquid water from the rest of the fuel cell components, images taken during cell operation were normalised to a dry fuel cell image taken at the beginning of each experiment. δ_{water}, the total water thickness of each image, could be calculated using the following equation by inverting the Beer-Lambert law:

$$\delta_{water} = -\frac{\ln(I / I_0)}{\varepsilon_{water}} \tag{1}$$

where ε_{water} refers to the attenuation coefficient of neutrons in liquid water, measured in the given setup at 5.3 cm^{-1}, I_0 is the intensity of the reference image (without water), which was taken after the dry gas was flowing through both sides of the cell for 10 min before each experiment. While I refers to the intensity of the 'working' image, which was taken during cell operation.

3. Results and discussion

To study the effect of compression on the cell performance, current sweep experiments were carried out in steps of 50 mA cm^{-2} for 10 min per point from 50 to 1100 mA cm^{-2} until the voltage fell below 0.4 V. Each polarisation was repeated twice and averaged. The corresponding cell current density, voltage and neutron imaging results were recorded simultaneously.
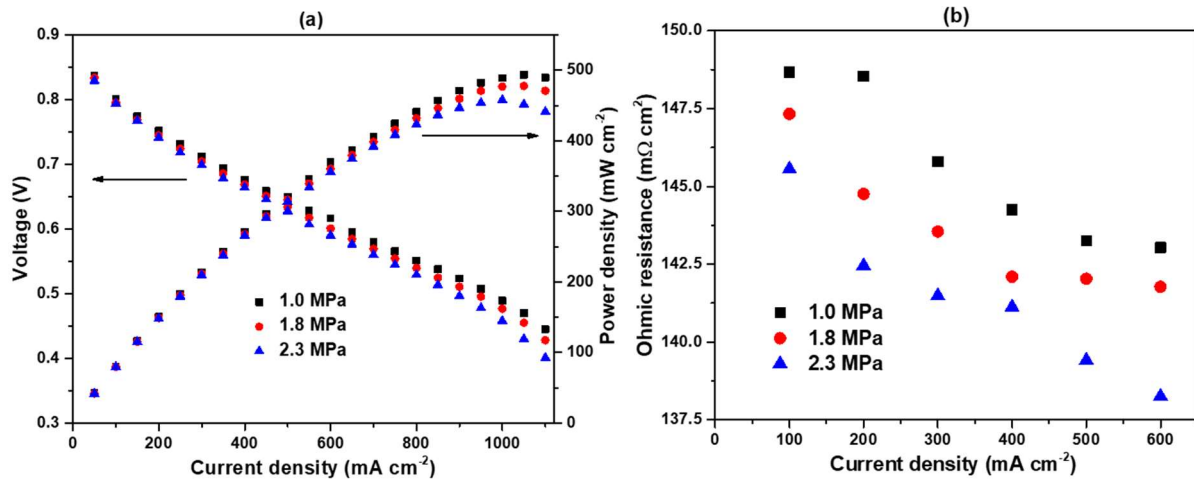
Fig.2 Effect of compression (1.0, 1.8 and 2.3 MPa) on (a) polarisation performance and (b) ohmic resistance.

Fig. 2 (a) compares the cell performance under different compression pressure. In general, the cell with higher compression pressure tends to perform worse, which agrees with other experimental studies [5]-[7]. At low current densities ($\leqslant 200$ mA cm^{-2}), the performance difference between the three compression pressures is minimal, but diverges with increasing current density. The cell compressed at 1.0 MPa exhibits ~0.4% and ~0.9% increase in performance over 1.8 MPa and 2.3 MPa at 50 mA cm^{-2}, and ~3.8% and ~9.9% at 1100 mA cm^{-2}, respectively. Fig. 2 (a) shows a decrease in maximum power density in the PEFC compressed at higher pressure, with the highest value recorded at a cell compressed at 1.0 MPa (491.4 mW cm^{-2}), followed by 1.8 MPa (478.9 mW cm^{-2}) and 2.3 MPa (458.0 mW cm^{-2}). The performance deviation in the mass transport region is possibly due to flooding or its resultant fuel starvation. Another possible explanation could be due to the loss of the porosity of the GDL under the land at higher compression pressure [10]-[13]. Both effects could contribute to the loss of performance.

Fig. 2 (b) shows the ohmic resistance as a function of average current density. In all cases, a higher current density results in a decrease in ohmic resistance as the membrane hydrates more from elevated water generation. Additionally, the increasing compression pressure lead to the decrease of ohmic resistance and this is associated with the improved contact between GDL and flow-field.

This implies that there are two competing factors working in opposition: High compression pressure could reduce the cell ohmic resistance, but on the other hand, it renders the loss of the porosity of the

GDL under the land and worsen the water accumulation in the PEFC, leading to the higher mass transport resistance [5]. Therefore, it is a trade-off between ohmic resistance and the mass transport resistance. However, because the mass transport resistance is significantly larger than the ohmic resistance [5], it is therefore recommended that a minimum cell compression is required to ensure gas-tight operation and reduced ohmic resistance, above which further compression leads to mass transfer limitations and cell performance decrease.

A set of neutron radiographs are presented in Fig. 3 in order to visualise the water evolution with time in the cell. The PEFC was compressed at 1.0 MPa and operated galvanostatically at 600 mA cm^{-2} over 18 minutes. The original neutron radiographs (grey scale) were colored with a yellow/blue mask for guidance (where blue indicates liquid water).
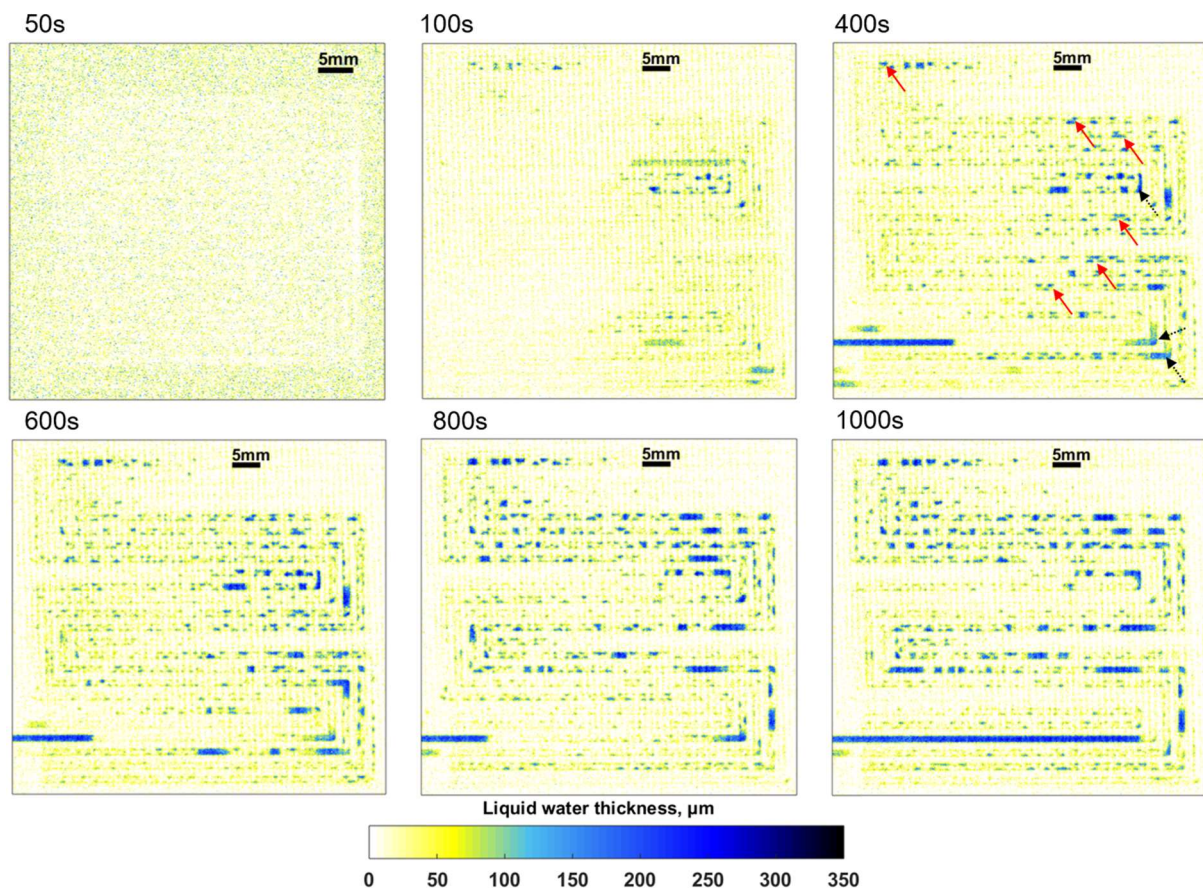

Fig. 3 Neutron image series of the water thickness distribution in the PEFC compressed at 1.0 MPa. The cell was operated at galvanostatic mode of 600 mA cm^{-2}.

The horizontal five-channel serpentine geometry of the cathode and vertical single-channel serpentine at the anode (as seen in Fig. 1 (b)) makes it possible to distinguish which electrode the water belongs to. Fig. 3a (~50 s after the current was first drawn) shows no water in the flow channels. This is due to the time required for water generated at the cathode to be transported through the GDL into the channels. Fig. 3b (~100 s) shows liquid water begins to emerge and distribute in the flow channels in the form of small droplets and surface film (85-220 μm). Fig. 3b shows that the water is not uniformly distributed across the active area and it mainly resides in the cathode (horizontal channels). This was identified in other neutron imaging studies [21], [23]-[28], [35], and is due to water that has been electrochemically generated at the cathode and that transported from the anode to cathode via electroosmotic drag. Water accumulation in the anode during dry gas operation only occurs when the rate of back-diffusion surpasses the rate of water removal [36], [37]. However, the stoichiometry (1.5 at the anode) used in the current test provides high gas velocity through the channel, leading to effective liquid water removal. Fig. 3c shows more liquid droplets appearing on the cathode channel walls (solid red arrows, 105-230 μm). One explanation for this is that the lands are cooler than the open-channel/GDL areas [27], [38]. Consequently, water vapor preferentially condenses under the land and liquid water starts protruding into the channel once the region under the land is saturated. Additionally, liquid water was observed around channel bends (dashed black arrows, 120-260 μm). This is a well-known feature of serpentine flow-fields [39]-[41], and it is attributed to the decreasing channel-to-channel pressure gradient near the bend and /or flow detachment/instability. With time, water accumulation slows down and approaches steady-state condition, as seen in Fig. 3 (d-f).

Fig. 4 (a) compares the averaged liquid water thickness distribution (rather than a particular time) in the PEFCs under different compression pressures (1.0 MPa, 1.8 MPa and 2.3 MPa, respectively) operated galvanostatically at 600 mA cm^{-2} (average current density) over 18 minutes. An increase in water accumulation with compression pressure is observed, with the highest liquid water accumulation recorded at a cell compression of 2.3 MPa (110-370 μm), followed by 1.8 MPa (110-325 μm) and 1.0 MPa (105-280 μm).
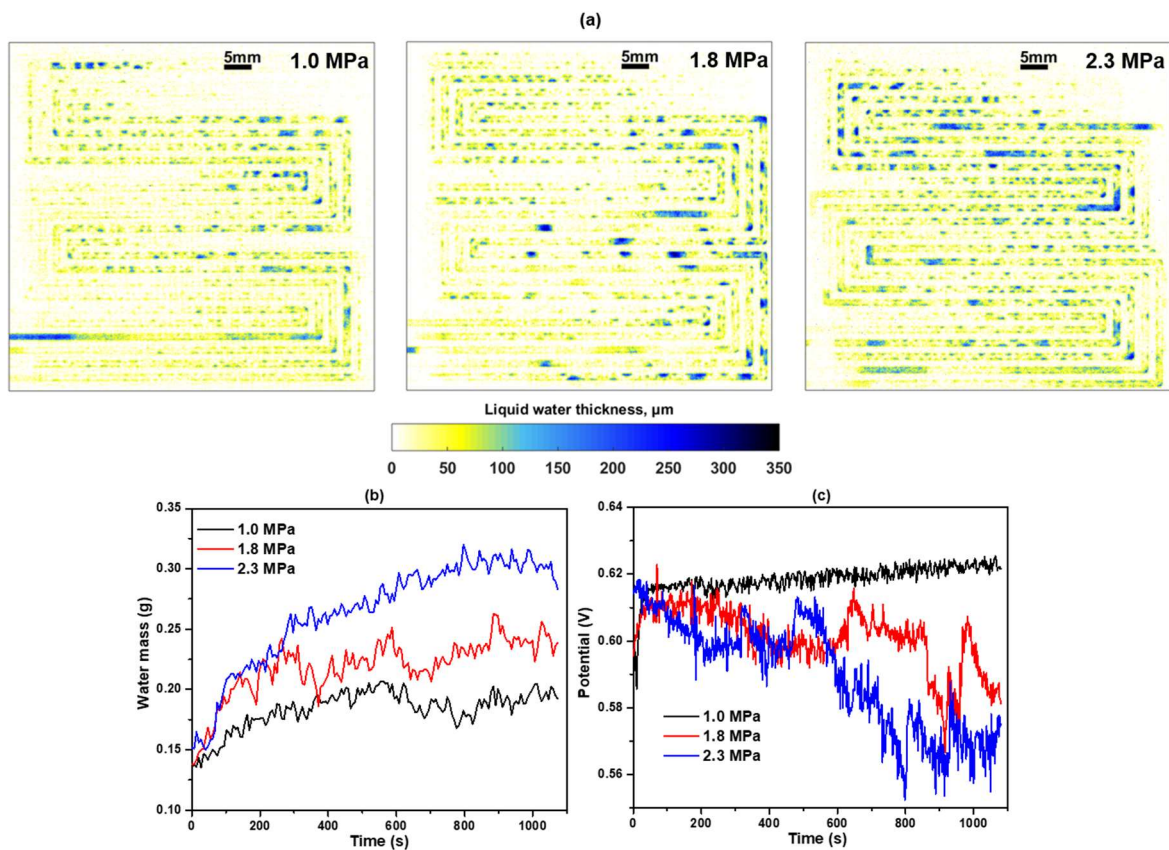
Fig. 4 Effect of compression (1.0, 1.8 and 2.3 MPa) on (a) averaged liquid water thickness distribution, (b) evolution of accumulated water mass and (c) potential during galvanostatic operation at 600 mA cm^{-2}.

The mass of accumulated liquid water in the PEFC was calculated from the averaged neutron image by integrating the localised water thickness across the entire active area to evaluate the effect of compression on total liquid water content. For example, a 25 cm^2 active area PEFC will generate a water mass of 1.51 g after 18 min of galvanostatic operation at 600 mA cm^{-2} (average current density).

As seen in Fig. 4 (b), in comparison to the cell compressed at 1.8 MPa and 2.3 MPa, which exhibited significant liquid water accumulation, much less water is present in the cell compressed at 1.0 MPa for the duration of the current hold. The total mass of accumulated liquid water in the cell compressed at 1.8 and 2.3 MPa exhibits ~19.5% and ~44.1% increase, compared to the cell compressed at 1.0 MPa. The result indicates an elevated susceptibility to flooding with increased compression pressure.

One feature shared amongst the three compression pressures is that the dynamics of water accumulation, which comprises three main stages: a first stage with slow water accumulation (< 50 s), a second stage

with rapid water accumulation (50 s ≤ t ≤ 300 s), and third stage approaching steady-state condition where the water accumulation slows down or slightly decreases (> 300 s). This trend agrees with a previous study which examined the liquid water build-up and the time evolution recorded by neutron radiography [35].

Removal and prevention of liquid water build-up in the PEFC is required to maintain a steady and reliable performance. Fig. 4 (c) shows the voltage evolution of each cell with different compression pressure during galvanostatic operation at 600 mA cm^{-2}. Correlation of performance to neutron radiography reveals that the accumulation of excessive liquid water in the cell compressed at 1.8 MPa and 2.3 MPa is the cause of flooding and subsequent performance deterioration. The cell compressed at 2.3 MPa showed severe performance deterioration after 440 s, revealing ineffective liquid water removal. On the contrary, the cell compressed at 1.0 MPa exhibits higher and more stable performance as a result of effective water management. This feature is in agreement with Fig. 4 (a), which shows that more liquid water accumulates at higher compression. It is anticipated that the liquid water removal is partially impeded due to the loss of the porosity and increased tortuosity factor of the GDLs at higher compression pressure. Compression also affect the capillary transport in the GDL. This relationship could be extracted using the Young-Laplace equation [42], [43]:

$$P_c = (\frac{2\gamma}{r})\cos\theta \tag{2}$$

where r is the pore radius of GDL, γ the surface tension and θ the contact angle of liquid water on the solid surface of the GDL pore wall.

This implies that capillary pressure is inversely proportional to the pore radius of GDL. Therefore, higher compression pressure leads to the smaller pore radius of GDL [10] and consequent higher capillary pressure, hindering effective water removal from the PEFC.

The emergence of excess liquid water into the gas channels can induce local blockage of gas channels and hinder reactant transport [44]. Therefore, a detailed quantitative investigation of the water droplet number and droplet surface area in the flow channels is of value. To this end, liquid water needed to be

segmented from the 'raw' neutron images. Here, the post-processing and image segmentation were performed using Avizo 9.0 software (Thermo Fisher Scientific, US). The averaged liquid water thickness distribution (compressed at 1.0 MPa) during constant current operation over 18 minutes at 600 mA cm^{-2} (same as the one on the left of Fig. 4(a)) is given on the left of Fig. 5 as a sample image.
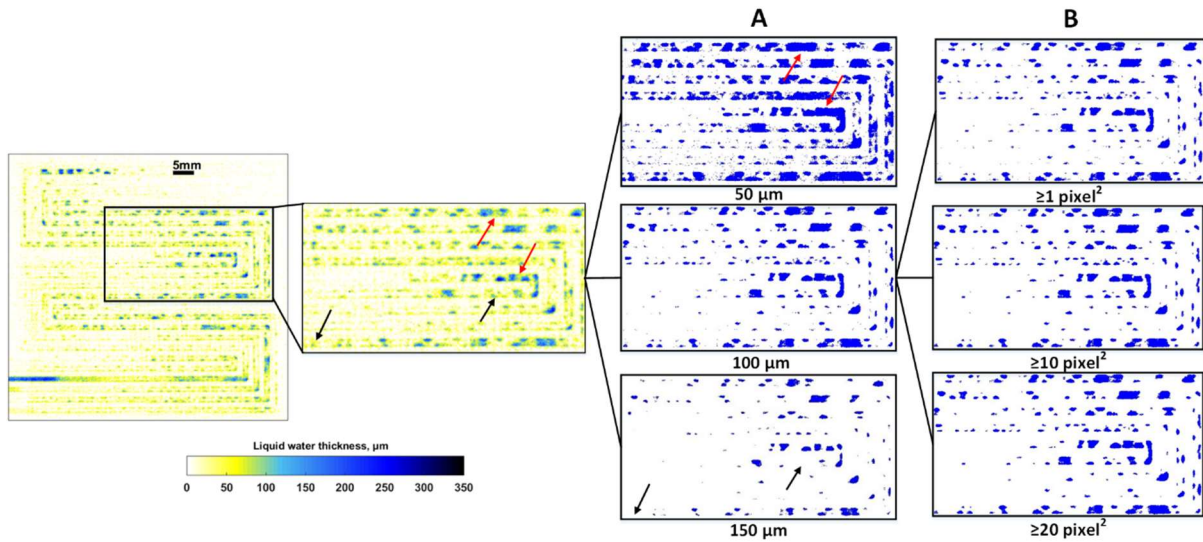

Fig. 5 Determination of suitable parameters for the quantitative investigation of the water droplet number and surface area. A sample neutron image was given on the left (both the complete cell and a magnified cut out). Right: Cut out of detected droplets using (A) three different threshold values for the water thickness and (B) three different values of the minimum pixel-based area with a threshold thickness of 100 μm.

The threshold algorithm in Avizo was used to segment the water droplet from the filtered sample image. By applying a threshold for the water thickness, any water droplets with thickness above this value were sieved. The thickness value must be chosen appropriately. On the one hand, it is not possible to distinguish single water droplets from one another for unreasonably small thickness (see red arrows in Fig. 5 A). On the other hand, if the threshold is too high, some water droplets shown in the sample image no longer appear in the resulting images (see black arrows in Fig. 5 A). The effect of different thickness is shown in Fig. 5 A. As a good compromise, a threshold value of 100 μm has been used for the sample image. A minimum lateral pixel-based area was chosen to select the water droplet and further remove the noise. This value was set to 10 pixels (equivalent to 6.76×10^3 μm^2). The effect of different pixel numbers can be seen in Fig. 5 B.

Note that a water droplet was only selected if both criteria have been satisfied: The thickness of the water droplet is above 100 μm and its lateral pixel-based area is larger than 6.76×10^3 μm^2, which means not all the water is shown in the sample image fits. This method is suitable for qualitative investigation of droplet size distributions and the transport behaviour from the GDL into the channel, which has been employed to study the effect of ageing of GDL on the water distribution in flow-field channels of PEFCs, for example [45].

Subsequently, the number and surface area of the water droplets in the flow channels of PEFCs compressed at different pressure are determined with the 'label analysis' function in Avizo. The data in Fig. 6 is based on the averaged liquid water thickness distribution (compressed at 1.0, 1.8 and 2.3 MPa respectively) during constant current operation over 18 minutes at 600 mA cm^{-2} (same as Fig. 4(a)). The median of the droplet size distribution is indicated by a solid black line in Fig. 6 (a), whereby 50% of the water surface area appears in smaller and 50% in larger droplets. The median droplet surface area in the cell compressed at 1.8 and 2.3 MPa demonstrates ~12.9% and ~76.9% increase, compared to the cell compressed at 1.0 MPa, meaning that larger water agglomerations form with increased compression pressure. Besides, the dashed red line in Fig. 6 (a) reveal that the number of water droplets in the cell compressed at 1.8 and 2.3 MPa demonstrates a ~21.2% and ~61.2% increase, compared to the cell compressed at 1.0 MPa, indicating ineffective water removal.
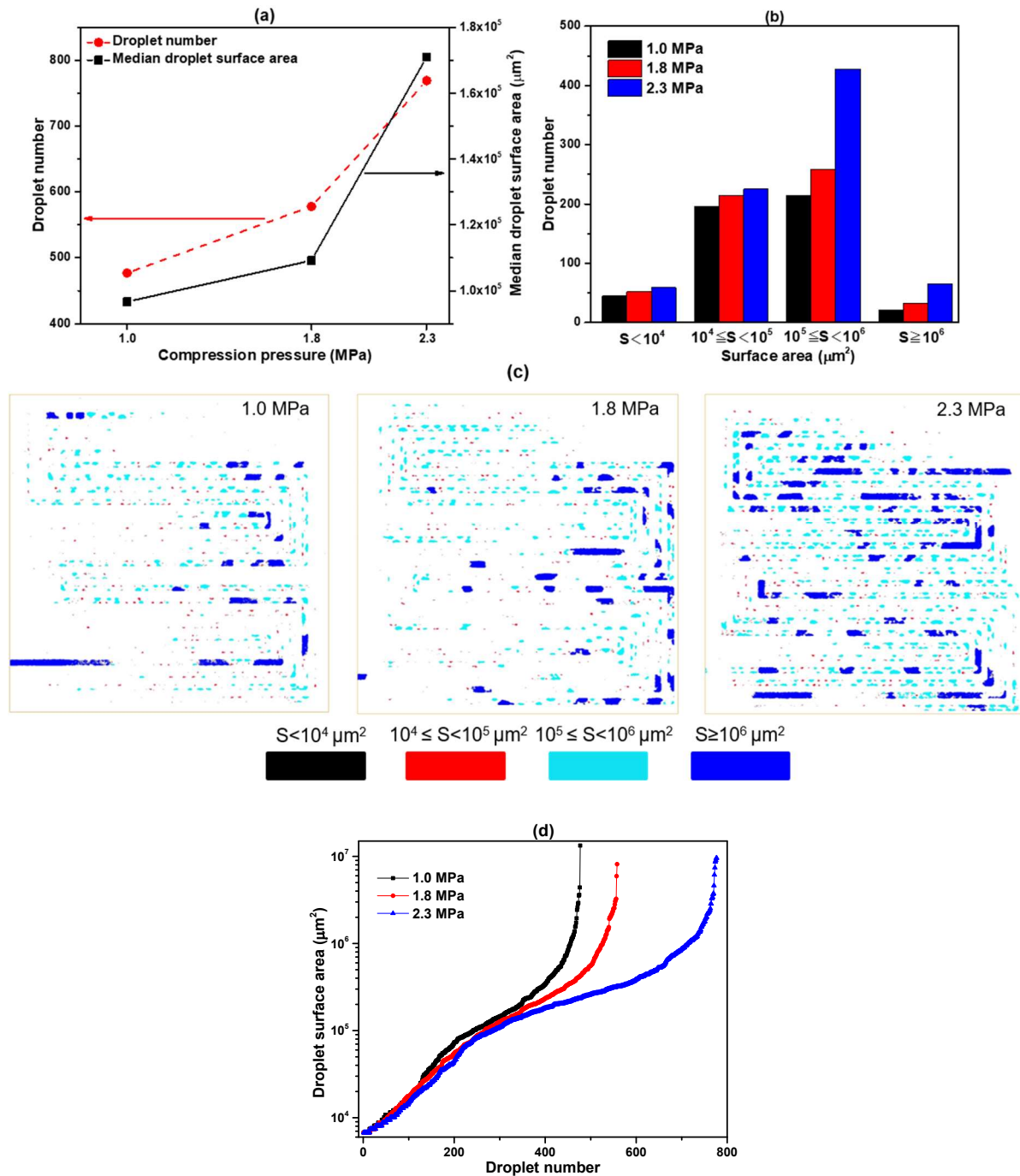
Fig. 6 Effect of compression on droplet number and median surface area (a), droplet surface area distribution in four classes (b), their corresponding location (c) and distribution of droplet surface areas in size order (d). The 'S' in (b) and (c) denotes surface area of droplets.

Fig. 6 (b) shows the effect of cell compression pressure on the droplet surface area distribution. The water droplets are categorized into four classes according to their surface area. The number of droplets within the four surface area classes is plotted on the ordinate axis. Fig. 6(b) shows the surface area of most droplets (86%, 85% and 84% of droplets in cells compressed at 1.0 MPa, 1.8 MPa and 2.3 MPa,

respectively) falls within the range of 10^4 to 10^6 μm^2, which is similar to the droplet size distribution in [45]. Fig. 6 (b) also indicates that the higher compression pressure leads to more droplets in all the four different surface area classes. Furthermore, the 'sieve' function implemented in Avizo was employed to group averaged liquid water distribution in the cell compressed at different pressures into the same classes in Fig. 6(b). The corresponding location of droplets is shown in Fig. 6(c).

Some general points can be noted about the nature of the droplets falling into each size category. For $<10^4$ μm^2, these droplets are difficult to distinguish in the figure as printed, but are mainly composed of a thin film primarily located at channel wall locations. For 10^4 to 10^5 μm^2, the drops are approximately spherical in shape and also located at channel wall locations. These drops could be considered to be the seeds of the larger drops (10^5 to 10^6 μm^2) that are still located at the channel wall boundaries but have grown / coalesced to form elongated slugs. Finally, the drops above 10^6 μm represent areas where the channel width is completely filled with liquid water; a greater proportion of the channels are filled over time.

While there is a common trend of greater number of water droplets formed in each droplet size category with increasing cell compression, the $<10^4$ μm^2 and 10^4 to 10^5 μm^2 ranges are similar in the amounts of water present for each droplet size. Fig. 6(d) shows the distribution of droplet areas in size order for each cell compression. It can be seen that the smallest ~340 drops in all cell compressions have the similar surface area size distribution (up to ~2×10^5 μm^2). However, beyond this number, significantly more drops form in the larger size ranges with increasing cell compression.

There are a number of possible reasons for this drop-size dependence with cell compression behaviour, involving mechanisms under the lands and in the channels. As the cell is compressed, two general things occur: the GDL under the land thins and the porosity is reduced; the GDL under the open channel protrudes into the channel in a process known as 'tenting'[5]. Increased compression reduces the ability of the GDL under the land to accommodate water, making it more likely to eject into the channel. The protrusion of GDL fibers into the channel forms a 'groove' at the interface with the side channel walls which can accommodate liquid water pooling more effectively. Additionally, given the GDL fibers

entrance into the channel, the channel depth is reduced, and therefore a same volume of water will be expanded in the channel direction resulting in elongated slugs.

Graphite based flow-fields are used in this study, making the system representative of many fuel cell systems. However, it is well known that the nature of the channel wall material (specifically its roughness, and hydrophilic/phobic nature, can affect the way in which water wets and accumulates in channels [46], [47]. This must, therefore, be considered when considering the water management of any given system.

Conclusion

The liquid water distribution and transport within a PEFC under different compression pressures has been investigated using in-operando neutron radiography. Subsequently, a quantitative analysis is presented with the influence of compression pressure on the water droplet number and median droplet surface area across the entire active cell area. This study provides, for the first time, unequivocal experimental validation of previously conducted numerical simulation and ex-situ measurements of the effect of water management in PEFCs as a function of cell compression.

The results revealed that the water management and performance of PEFCs is strongly affected by compression: the cell compressed at 1.0 MPa demonstrates ~3.2% and ~7.8% increase in maximum power density over 1.8 MPa and 2.3 MPa, respectively. Correlation of performance to neutron radiography reveals that the performance deviation in the mass transport region is likely due to flooding issues or its resultant fuel starvation. During galvanostatic operation at 600 mA cm^{-2}, the averaged mass of accumulated liquid water in the cell compressed at 1.8 and 2.3 MPa demonstrates ~19.5% and ~44.1% increase, compared to the cell compressed at 1.0 MPa. This is possibly ascribed to the loss of the porosity and increased tortuosity factor of GDL fibre microstructure under channel lands and protrusion of GDL fibres into open channels. Furthermore, greater insight has been gained about the size, number and location of droplet formation as a function of cell compression. The median droplet surface area in the cell compressed at 1.8 and 2.3 MPa demonstrates ~12.9% and ~76.9% increase, compared to the cell compressed at 1.0 MPa. As for the water droplet number, it increases by ~21.2% and ~61.2%

compared to 1.0 MPa, indicating the liquid water removal is partially impeded at higher compression pressure. It is therefore recommended that a minimum cell compression is required to ensure gas-tight operation and reduced contact resistance, above which further compression leads to excess water accumulation and mass transfer limitations.

Acknowledgements

References

[1] Mehta, V. and Cooper, J.S. "Review and analysis of PEM fuel cell design and manufacturing." Journal of Power Sources 114.1 (2003): 32-53.

[2] Tolj, I., Bezmalinovic, D. and Barbir, F. "Maintaining desired level of relative humidity throughout a fuel cell with spatially variable heat removal rates." international journal of hydrogen energy 36.20 (2011): 13105-13113.

[3] Curtin, D.E., Lousenberg, R.D., Henry, T.J., Tangeman, P.C. and Tisack, M.E., "Advanced materials for improved PEMFC performance and life." Journal of power Sources 131.1-2 (2004): 41-48.

[4] Millichamp, J., Mason, T.J., Neville, T.P., Rajalakshmi, N., Jervis, R., Shearing, P.R. and Brett, D.J. "Mechanisms and effects of mechanical compression and dimensional change in polymer electrolyte fuel cells–A review." Journal of Power Sources 284 (2015): 305-320.

[5] Mason, T.J., Millichamp, J., Shearing, P.R. and Brett, D.J. "A study of the effect of compression on the performance of polymer electrolyte fuel cells using electrochemical impedance spectroscopy and dimensional change analysis." International journal of hydrogen energy 38.18 (2013): 7414-7422.

[6] Ge, J., Higier, A. and Liu, H. "Effect of gas diffusion layer compression on PEM fuel cell performance." Journal of Power Sources 159.2 (2006): 922-927.

[7] Chang, W.R., Hwang, J.J., Weng, F.B. and Chan, S.H. "Effect of clamping pressure on the performance of a PEM fuel cell." Journal of Power Sources 166.1 (2007): 149-154.

[8] Zhou, P., Wu, C.W. and Ma, G.J. "Influence of clamping force on the performance of PEMFCs." Journal of Power Sources 163.2 (2007): 874-881.

[9] Cha, D., Ahn, J.H., Kim, H.S. and Kim, Y. "Effects of clamping force on the water transport and performance of a PEM (proton electrolyte membrane) fuel cell with relative humidity and current density." Energy 93 (2015): 1338-1344.

[10] Tötzke, C., Gaiselmann, G., Osenberg, M., Bohner, J., Arlt, T., Markötter, H., Hilger, A., Wieder, F., Kupsch, A., Müller, B.R. and Hentschel, M.P. "Three-dimensional study of compressed gas diffusion layers using synchrotron X-ray imaging." Journal of Power Sources 253 (2014): 123-131.

[11] Khajeh-Hosseini-Dalasm, N., Sasabe, T., Tokumasu, T. and Pasaogullari, U. "Effects of polytetrafluoroethylene treatment and compression on gas diffusion layer microstructure using high-resolution X-ray computed tomography." Journal of Power Sources 266 (2014): 213-221.

[12] Zenyuk, I.V., Parkinson, D.Y., Connolly, L.G. and Weber, A.Z. "Gas-diffusion-layer structural properties under compression via X-ray tomography." Journal of Power Sources 328 (2016): 364-376.

[13] Banerjee, R., Hinebaugh, J., Liu, H., Yip, R., Ge, N. and Bazylak, A. "Heterogeneous porosity distributions of polymer electrolyte membrane fuel cell gas diffusion layer materials with rib-channel compression." International Journal of Hydrogen Energy 41.33 (2016): 14885-14896.

[14] Fazeli, M., Hinebaugh, J., Fishman, Z., Tötzke, C., Lehnert, W., Manke, I. and Bazylak, A. "Pore network modeling to explore the effects of compression on multiphase transport in polymer electrolyte membrane fuel cell gas diffusion layers." Journal of Power Sources 335 (2016): 162-171.

[15] Medici, E.F., Zenyuk, I.V., Parkinson, D.Y., Weber, A.Z. and Allen, J.S. "Understanding Water Transport in Polymer Electrolyte Fuel Cells Using Coupled Continuum and Pore-Network Models." Fuel Cells 16.6 (2016): 725-733.

[16] Rama, P., Liu, Y., Chen, R., Ostadi, H., Jiang, K., Gao, Y., Zhang, X., Brivio, D. and Grassini, P. "A numerical study of structural change and anisotropic permeability in compressed carbon cloth polymer electrolyte fuel cell gas diffusion layers." Fuel Cells 11.2 (2011): 274-285.

[17] Zenyuk, I.V., Parkinson, D.Y., Hwang, G. and Weber, A.Z. "Probing water distribution in compressed fuel-cell gas-diffusion layers using X-ray computed tomography." Electrochemistry Communications 53 (2015): 24-28.

[18] Ince, U.U., Markötter, H., George, M.G., Liu, H., Ge, N., Lee, J., Alrwashdeh, S.S., Zeis, R., Messerschmidt, M., Scholta, J. and Bazylak, A. "Effects of compression on water distribution in gas diffusion layer materials of PEMFC in a point injection device by means of synchrotron X-ray imaging." International Journal of Hydrogen Energy 43.1 (2018): 391-406.

[19] Jeon, D.H. and Kim, H. "Effect of compression on water transport in gas diffusion layer of polymer electrolyte membrane fuel cell using lattice Boltzmann method." Journal of Power Sources 294 (2015): 393-405.

[20] Bazylak, A., Sinton, D., Liu, Z.S. and Djilali, N. "Effect of compression on liquid water transport and microstructure of PEMFC gas diffusion layers." Journal of Power Sources 163.2 (2007): 784-792.

[21] Satija, R., Jacobson, D.L., Arif, M. and Werner, S.A. "In situ neutron imaging technique for evaluation of water management systems in operating PEM fuel cells." Journal of Power Sources 129.2 (2004): 238-245.

[22] Mosdale, R., Gebel, G. and Pineri, M. "Water profile determination in a running proton exchange membrane fuel cell using small-angle neutron scattering." Journal of Membrane Science 118.2 (1996): 269-277.

[23] Y. Wu, J. I. S. Cho, T. P. Neville, Q. Meyer, R. Zeische, P. Boillat, M. Cochet, P. R. Shearing, and D. J. L. Brett. "Effect of serpentine flow-field design on the water management of polymer electrolyte fuel cells: An in-operando neutron radiography study." Journal of Power Sources 399 (2018): 254-263.

[24] Meyer, Q., Ashton, S., Jervis, R., Finegan, D.P., Boillat, P., Cochet, M., Curnick, O., Reisch, T., Adcock, P., Shearing, P.R. and Brett, D.J. "The Hydro-electro-thermal Performance of Air-cooled, Open-cathode Polymer Electrolyte Fuel Cells: Combined Localised Current Density, Temperature and Water Mapping." Electrochimica Acta 180 (2015): 307-315.

[25]   Murakawa, H., Sugimoto, K., Kitamura, N., Sawada, M., Asano, H., Takenaka, N. and Saito, Y. "Visualization of water accumulation process in polymer electrolyte fuel cell using neutron radiography." Physics Procedia 69 (2015): 607-611.

[26]   Iranzo, A., Boillat, P., Biesdorf, J. and Salva, A. "Investigation of the liquid water distributions in a 50 cm^2 PEM fuel cell: Effects of reactants relative humidity, current density, and cathode stoichiometry." Energy 82 (2015): 914-921.

[27]   Meyer, Q., Ashton, S., Boillat, P., Cochet, M., Engebretsen, E., Finegan, D.P., Lu, X., Bailey, J.J., Mansor, N., Abdulaziz, R. and Taiwo, O.O. "Effect of gas diffusion layer properties on water distribution across air-cooled, open-cathode polymer electrolyte fuel cells: A combined ex-situ X-ray tomography and in-operando neutron imaging study." Electrochimica Acta 211 (2016): 478-487.

[28]   Iranzo, A., Boillat, P., Salva, A. and Biesdorf, J. "PEM fuel cell operation under air and O2 feed: analysis of cell performance and liquid water distributions." Fuel Cells 16.4 (2016): 463-468.

[29]   Owejan, J.P., Trabold, T.A., Jacobson, D.L., Arif, M. and Kandlikar, S.G. "Effects of flow field and diffusion layer properties on water accumulation in a PEM fuel cell." International Journal of Hydrogen Energy 32.17 (2007): 4489-4502.

[30]   Yoshizawa, K., Ikezoe, K., Tasaki, Y., Kramer, D., Lehmann, E.H. and Scherer, G.G. "Analysis of gas diffusion layer and flow-field design in a PEMFC using neutron radiography." Journal of The Electrochemical Society 155.3 (2008): B223-B227.

[31]   Meyer, Q., Mansor, N., Iacoviello, F., Cullen, P.L., Jervis, R., Finegan, D., Tan, C., Bailey, J., Shearing, P.R. and Brett, D.J.L. "Investigation of hot pressed polymer electrolyte fuel cell assemblies via X-ray computed tomography." Electrochimica Acta 242 (2017): 125-136.

[32]   Movahedi, M., Ramiar, A. and Ranjber, A.A. "3D numerical investigation of clamping pressure effect on the performance of proton exchange membrane fuel cell with interdigitated flow field." Energy 142 (2018): 617-632.

[33]   Chen, C.C., Shaw, D. and Hsueh, K.L. "Optimization of the electrodes humidification temperature and clamping pressure to achieve uniform current density in a commercial-sized proton exchange membrane fuel cell." International Journal of Hydrogen Energy 42.5 (2017): 3185-3196.

[34]   Kardjilov, N., Hilger, A. and Manke, I. "Conrad-2: cold neutron tomography and radiography at ber ii (v7)." Journal of large-scale research facilities JLSRF 2 (2016): 98.

[35]   Iranzo, A., Salva, A., Boillat, P., Biesdorf, J., Tapia, E. and Rosa, F. "Water build-up and evolution during the start-up of a PEMFC: Visualization by means of Neutron Imaging." International Journal of Hydrogen Energy 42.19 (2017): 13839-13849.

[36]   Brett, D.J.L., Atkins, S., Brandon, N.P., Vasileiadis, N., Vesovic, V. and Kucernak, A.R. "Membrane resistance and current distribution measurements under various operating conditions in a polymer electrolyte fuel cell." Journal of power sources 172.1 (2007): 2-13.

[37]   Iranzo, A. and Boillat, P. "Liquid water distribution patterns featuring back-diffusion transport in a PEM fuel cell with neutron imaging." International Journal of Hydrogen Energy 39.30 (2014): 17240-17245.

[38]   Boillat, P. Advanced characterization of polymer electrolyte fuel cells using high resolution neutron imaging. Diss. ETH Zurich, 2009.

[39]   Trabold, T.A., Owejan, J.P., Jacobson, D.L., Arif, M. and Huffman, P.R. "In situ investigation of water transport in an operating PEM fuel cell using neutron radiography: Part 1–Experimental method and serpentine flow field results." International Journal of Heat and Mass Transfer 49.25-26 (2006): 4712-4720.

[40]   Suresh, P.V., Jayanti, S., Deshpande, A.P. and Haridoss, P. "An improved serpentine flow field with enhanced cross-flow for fuel cell applications." International journal of hydrogen energy 36.10 (2011): 6067-6072.

[41]   Ferreira, R.B., Falcão, D.S., Oliveira, V.B. and Pinto, A.M.F.R. "1D+ 3D two-phase flow numerical model of a proton exchange membrane fuel cell." Applied Energy 203 (2017): 474-495.

[42]   Gostick, J.T., Fowler, M.W., Ioannidis, M.A., Pritzker, M.D., Volfkovich, Y.M. and Sakars, A. "Capillary pressure and hydrophilic porosity in gas diffusion layers for polymer electrolyte fuel cells." Journal of power sources 156.2 (2006): 375-387.

[43]   Hao, L. and Cheng, P. "Capillary pressures in carbon paper gas diffusion layers having hydrophilic and hydrophobic pores." International Journal of Heat and Mass Transfer 55.1-3 (2012): 133-139.

[44]   Zhu, X., Sui, P.C. and Djilali, N., 2007. "Dynamic behaviour of liquid water emerging from a GDL pore into a PEMFC gas flow channel." Journal of Power Sources 172.1 (2007): 287-295.

[45]   Kätzel, J., Markötter, H., Arlt, T., Klages, M., Haußmann, J., Messerschmidt, M., Kardjilov, N., Scholta, J., Banhart, J. and Manke, I. "Effect of ageing of gas diffusion layers on the water distribution in flow field channels of polymer electrolyte membrane fuel cells." Journal of Power Sources 301 (2016): 386-391.

[46]   Cho, J. I. S., Neville T. P., Trogadas P, Meyer Q, Wu Y, Ziesche R, Boillat P, Cochet M, Shearing P, Brett D. J. L and Coppens M.-O, "Visualization of Liquid Water in a Lung-Inspired Flow-Field based Polymer Electrolyte Membrane Fuel Cell via Neutron Radiography." Energy. Under review.

[47]   Lu, Z., Rath, C., Zhang, G. and Kandlikar, S.G. "Water management studies in PEM fuel cells, part IV: Effects of channel surface wettability, geometry and orientation on the two-phase flow in parallel gas channels." International Journal of Hydrogen Energy 36.16 (2011): 9864-9875.